On the Quantification of Atmospheric Rivers Precipitation from Space: Composite Assessments and Case Studies over the Eastern North Pacific Ocean and the Western United States

ALI BEHRANGI

Jet Propulsion Laboratory, California Institute of Technology, Pasadena, California

BIN GUAN

Joint Institute for Regional Earth System Science and Engineering, University of California, Los Angeles, Los Angeles, and Jet Propulsion Laboratory, California Institute of Technology, Pasadena, California

PAUL J. NEIMAN

NOAA/Earth System Research Laboratory, Boulder, Colorado

MATHIAS SCHREIER AND BJORN LAMBRIGTSEN

Jet Propulsion Laboratory, California Institute of Technology, Pasadena, California

(Manuscript received 22 April 2015, in final form 18 September 2015)

ABSTRACT

Atmospheric rivers (ARs) are often associated with extreme precipitation, which can lead to flooding or alleviate droughts. A decade (2003–12) of landfalling ARs impacting the North American west coast (between 32.5° and 52.5°N) is collected to assess the skill of five commonly used satellite-based precipitation products [T3B42, T3B42 real-time (T3B42RT), CPC morphing technique (CMORPH), PERSIANN, and PERSIANN–Cloud Classification System (CCS)] in capturing ARs' precipitation rate and pattern. AR detection was carried out using a database containing twice-daily satellite-based integrated water vapor composite observations. It was found that satellite products are more consistent over ocean than land and often significantly underestimate precipitation rate over land compared to ground observations. Incorrect detection of precipitation from IR-based methods is prevalent over snow and ice surfaces where microwave estimates often show underestimation or missing data. Bias adjustment using ground observation is found very effective to improve satellite products, but it also raises concern regarding near-real-time applicability of satellite products for ARs. The analysis using individual case studies (6–8 January and 13–14 October 2009) and an ensemble of AR events suggests that further advancement in capturing orographic precipitation and precipitation over cold and frozen surfaces is needed to more reliably quantify AR precipitation from space.

1. Introduction

Atmospheric rivers (ARs) refer to narrow channels of enhanced water vapor transport concentrated in the lower atmosphere (Zhu and Newell 1994; Ralph et al. 2004). Occupying less than 10% of the earth's circumference, ARs account for over 90% of the poleward water vapor transport at midlatitudes (Zhu and Newell 1998). While ARs occur globally, their impacts are most prominent when they make landfall and interact with the topography of the west coast areas of midlatitude continents [Gimeno et al. (2014), and references therein]. Often they are associated with extreme precipitation, which can lead to flooding (e.g., Ralph et al. 2006; Neiman et al. 2011; Lavers and Villarini 2013) but can also alleviate or ''bust'' ongoing drought conditions (Dettinger 2013).

The important hydrological effects of ARs have been widely documented in the semiarid western United

Corresponding author address: Ali Behrangi, Jet Propulsion Laboratory, California Institute of Technology, 4800 Oak Grove Dr., MS 233-304, Pasadena, CA 91109.
E-mail: ali.behrangi@jpl.nasa.gov

DOI: 10.1175/JHM-D-15-0061.1

States. About 30%–50% of annual precipitation in this region fell during ARs over the period of water years (WYs) 1998–2008 (Dettinger et al. 2011). On average, 6–7 ARs per winter account for 40% of the annual snow accumulation in California's Sierra Nevada during WYs 2004–10 (Guan et al. 2010, 2013). All seven major flooding events in California's Russian River basin during WYs 1998–2006 were associated with ARs (Ralph et al. 2006), as were 46 out of 48 annual peak daily flow events in Washington during WYs 1998–2009 (Neiman et al. 2011). Recently, it was found that 33%–74% of droughts in the western United States were broken by the arrival of ARs (Dettinger 2013), with the highest and lowest percent observed in Washington and southern coastal California, respectively. Similar hydrological importance of ARs has been indicated by studies focusing on Europe (Stohl et al. 2008; Lavers and Villarini 2013) and South America (Viale and Nuñez 2011). Together, these studies suggest the need to better observe and understand ARs and their impacts.

ARs are typically formed over midlatitude oceanic regions, and it often takes a few days for them to make landfall. Because of a lack of rain gauge and ground-radar over the ocean, an important alternative for retrieving precipitation from such systems is satellite, enabling observations of ARs throughout their entire life cycle (e.g., Matrosov 2012, 2013) and before they make landfall. Compared to many regions of the world, the western Unites States is fairly well instrumented and thus provides an opportunity to assess the weaknesses and strengths of satellite products in capturing AR precipitation events as they make landfall. The outcomes can help improve precipitation retrieval methods and provide insights on the reliability of satellite estimates over regions where ground observations are sparse or nonexistent.

Precipitation from ARs often possesses unique features. Compared to other winter storms, the lower tropospheric air temperature during AR precipitation is typically warmer with correspondingly higher melting levels (e.g., Neiman et al. 2008, 2011; Warner et al. 2012; Kim et al. 2013). Furthermore, once such systems make landfall they can be impacted by topography and generate substantial orographic precipitation. In the western United States, a large fraction of ARs occur in winter in the form of snowfall or rainfall over snow and ice surfaces. This makes it more difficult for retrieving precipitation from infrared (IR) and microwave (MW) sensors, both of which are commonly used in merged precipitation products (Huffman et al. 2007; Joyce et al. 2004; Hsu et al. 1997; Sorooshian et al. 2000; Kuligowski 2002; Behrangi et al. 2010). IR-based techniques are based on the general assumption that colder clouds statistically produce more intense rainfall, so the IR techniques have been known to miss heavy precipitation from shallow clouds and they have been prone to false detection of precipitation over ice and snow surface (Kidd et al. 2003; Behrangi et al. 2009). MW-based precipitation retrieval over land, however, relies mainly on scattering properties of ice particles, partly because quantification of emissivity over land is difficult and is an ongoing challenge (Ferraro et al. 2013). This has limited the performance of MW-based precipitation retrievals in capturing warm rainfall observed in many regions (Liu and Zipser 2009) including the North American west coast (e.g., Neiman et al. 2005; Martner et al. 2008). Furthermore, the presence of ice and snow on the surface adds more difficulties to MW-based precipitation retrieval methods, and often no retrieval is performed from MW imagers over snow and ice surfaces. MW sounders could be more effective in such situations as sensitivity of water vapor channels to surface emission is low and the high-frequency channels are effective in capturing scattering signals from cloud ice particles and snowflakes. For example, AMSU Microwave Humidity Sounder (MHS) precipitation from the Microwave Surface and Precipitation Products System (Ferraro et al. 2000; Weng et al. 2003; Vila et al. 2007) employs a technique (Kongoli et al. 2003; H. Meng et al. 2012, meeting presentation) through which a combination of MW sounding channels is used to distinguish between the scattering features over land surfaces (especially snow cover) and that of the atmosphere (precipitation-sized ice particles). However, a long-standing difficulty remains in dry atmospheres (e.g., total water vapor column of less than 10–15 mm), where even the 183-GHz sounding channels are heavily impacted by the surface.

Because of the important impacts of ARs on water resources across the western United States and the various potential challenges for satellite-based retrieval of precipitation over this region (e.g., snow, rain on snow, and orographic precipitation), the present study focuses on assessing the performance of the commonly used merged precipitation products in capturing precipitation from landfalling ARs originating over the eastern North Pacific Ocean. AR landfalls based on the less (more) stringent satellite-based AR criteria (see section 2) were used for comparison focusing on the ocean (land). The outcomes are expected to provide useful insights on the application of such datasets and future plans to improve the observing systems and products.

2. Dataset and study area

a. AR database

In this study, ARs are defined as satellite-observed integrated water vapor (IWV) plumes greater than

2000 km long, less than 1000 km wide, and with IWV greater than 20 mm. These AR criteria were established by Ralph et al. (2004) based on dropsonde observations of ARs and were later used by Neiman et al. (2008) to create an inventory of landfalling ARs on the west coast of North America between WYs 1998 and 2013. The inventory is based on examining twice-daily (ascending and descending passes) composite satellite images of IWV as observed by the Special Sensor Microwave Imager (SSM/I) and Special Sensor Microwave Imager/Sounder (SSMIS) instruments on Defense Meteorological Satellite Program (DMSP) satellites. California landfalls are defined as the dates when the IWV plume intersects the west coast between 32.5° and 41.0°N in either the ascending or descending satellite pass. Correspondingly, Pacific Northwest landfalls are defined as those intersecting the west coast between 41.0° and 52.5°N. A subset of the catalog based on the more stringent criteria (i.e., dates when ARs are intersecting the coast in both ascending and descending passes) is also used for analysis over land. The use of the more stringent AR landfall criteria for the land-focused analysis is to prevent the possible inclusion of partial days when the AR has not yet intersected the coast and therefore any overland impact has not yet been realized. Here, the California and the Pacific Northwest landfalls are referred to as ''south'' and ''north'' landfalls, respectively.

b. Precipitation dataset

1) PRISM

Reference precipitation data are obtained from the Parameter-Elevation Regressions on Independent Slopes Model (PRISM) dataset (Daly et al. 2002) developed by the PRISM Climate Group at Oregon State University. PRISM data are generated from high-quality meteorological stations interpolated to a 4-km grid using a human expert and statistical knowledge-based system (Daly et al. 2002; http://www.prism.oregonstate.edu). In other words, PRISM uses knowledge on the spatial patterns of climate and their relationships with geographic features to help enhance, control, and parameterize a statistical technique to create high-quality precipitation maps using gauge stations. A weighted climate–elevation regression function is also used to account for the influence of elevation on climate. Daily and monthly PRISM data are available over the continental United States (CONUS) for several decades. Daily products are used in this study.

2) SATELLITE PRODUCTS

The following satellite-based precipitation products are utilized in the present study: 1) Tropical Rainfall Measuring Mission (TRMM) 3B42 real-time (RT), version 7 (T3B42RT; Huffman et al. 2007); 2) TRMM 3B42 research product, version 7 (T3B42; Huffman et al. 2007; Huffman and Bolvin 2014); 3) Climate Prediction Center (CPC) morphing technique (CMORPH; Joyce et al. 2004); 4) Precipitation Estimation from Remotely Sensed Information Using Artificial Neural Networks (PERSIANN; Hsu et al. 1997; Sorooshian et al. 2000); and 5) PERSIANN–Cloud Classification System (PERSIANN-CCS, hereafter referred to as CCS; Hong et al. 2004). T3B42 combines various MW-derived precipitation estimates with MW-calibrated infrared estimates, and the final product is adjusted for bias using monthly gauge data. Note that T3B42 mainly uses the Global Precipitation Climatology Centre (GPCC) gauges, which are not as complete as those used in PRISM (e.g., PRISM uses several other sources, such as radars and SNOTEL, explained in the PRISM document). Furthermore, the bias adjustment in T3B42 is only applied to grids with a precipitation rate above zero. Therefore, while both products are adjusted by gauges, T3B42 and PRISM are not necessarily similar. On the other hand, T3B42RT only relies on climatology for bias adjustment to reduce data latency. Furthermore, in T3B42 the TRMM Combined Instrument (TCI) from the TRMM 2B31 product (Haddad et al. 1997) is used as a reference for the intercalibration of other MW precipitation estimates, while this is done by using the TRMM Microwave Imager in T3B42RT. T3B42 and T3B42RT are produced at 0.25° × 0.25° spatial resolution every 3 h and are available since 1998 and 2000, respectively. CMORPH produces a temporally and spatially complete precipitation field by interpolating the MW precipitation data along cloud tracks that are obtained entirely from geostationary satellite IR data. Therefore, CMORPH uses precipitation estimates exclusively from MW retrievals. The product is available at 0.25° × 0.25° spatial resolution every 3 h and 0.07° × 0.07° spatial resolution every 30 min. Both PERISANN and CCS derive precipitation from a single IR channel (~11 μm). PERSIANN is a pixel-based approach and MW precipitation data are used to update the parameters that relate IR to precipitation intensity, while CCS is a patch-based approach in which the relation between IR and precipitation rate is established for each class of cloud patches. PERISANN data are available since 2000 at 0.25° × 0.25° spatial resolution every hour, while CCS has been produced at 0.04° × 0.04° spatial resolution every 30 min since 2004. Our initial analysis using high-resolution products from CCS and CMORPH showed that the results presented in the work are not changed if higher-resolution products are used. Therefore, for consistency with the other products, we used

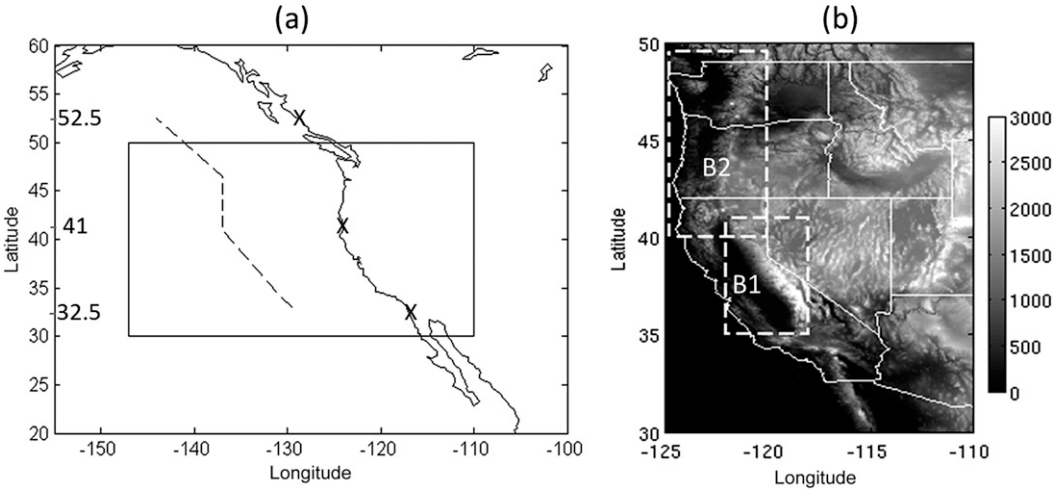

FIG. 1. The study region. (a) The solid box shows the study area and the dotted line (~1000 km offshore) bounds a North American west coast domain in which landfalling ARs are observed and collected in the AR database. (b) Topography map with elevation (m MSL). In (a) the latitude positions at 32.5°, 41.0°, and 52.5°N along the coast represent the boundaries of the south coast and north coast AR landfalls. In (b), dashed boxes B1 and B2 delineate two study areas discussed later in the present study.

0.25° × 0.25° spatial and daily temporal resolution in this study. Note that a PRISM day is defined as 1200–1200 UTC. This is considered in construction of comparable daily precipitation data from remote sensing products using 3-h precipitation maps.

c. *Auxiliary data*

Surface elevation and 2-m air temperature data are also utilized in this study to complement the analysis. Both datasets are obtained from PRISM. Similar to precipitation datasets, PRISM provides 4-km daily air temperature data over the CONUS. Elevation maps are also available at 800-m resolution grids. Both surface air temperature and elevation grids were mapped to 0.25° × 0.25° spatial resolution prior to the analysis.

3. Method

ARs can heavily impact the western United States with intense precipitation and flooding. In contrast, a lack of ARs can contribute to droughts. Therefore, for comparison of different precipitation products, both aspects of precipitation—total and rate (i.e., intensity)—have to be considered. Using the AR landfall database described in section 2, AR precipitation is determined from the various satellite-based precipitation products described in the previous section. Landfalls based on the less (more) stringent SSM/I- and SSMIS-based AR criteria (see section 2) were used for comparison focusing on the ocean (land). For comparison over land, precipitation data are collected for days on which ARs hit the coast, and the immediate day after those days, to include most of the precipitation events likely caused by ARs (Dettinger et al. 2011; Kim et al. 2013). The daily precipitation data are then compared by constructing geographical maps and probability density functions for precipitation intensity.

The study region (Fig. 1) includes mountainous areas with high elevations that can induce orographic precipitation and receive major snowfall during winter. Data from 10 calendar years (2003–12) are used in this study. Surface temperature is used as auxiliary information to distinguish snowfall from rainfall events. In other words, it was assumed that precipitation with a surface temperature of 0°C or lower falls as snow. While this distinction may not be accurate, it helps investigate how different products compare for cases that are likely snowfall at the surface. It should be noted that the 0°C threshold used in this study is likely conservative. For example, Lundquist et al. (2008) showed that in the free atmosphere the transition from snow to rain starts at 0° and at 1.5°C, 50% of precipitation events fall as rain and 50% as snow.

4. Results

Here the assessment is performed using long-term statistics, providing more reliable assessment, as well as two event-based case studies.

a. *10-yr composite analyses*

Figure 2 shows maps of mean AR precipitation rate based on the less stringent landfall criteria (see section 2). From left to right, the columns include only ARs that

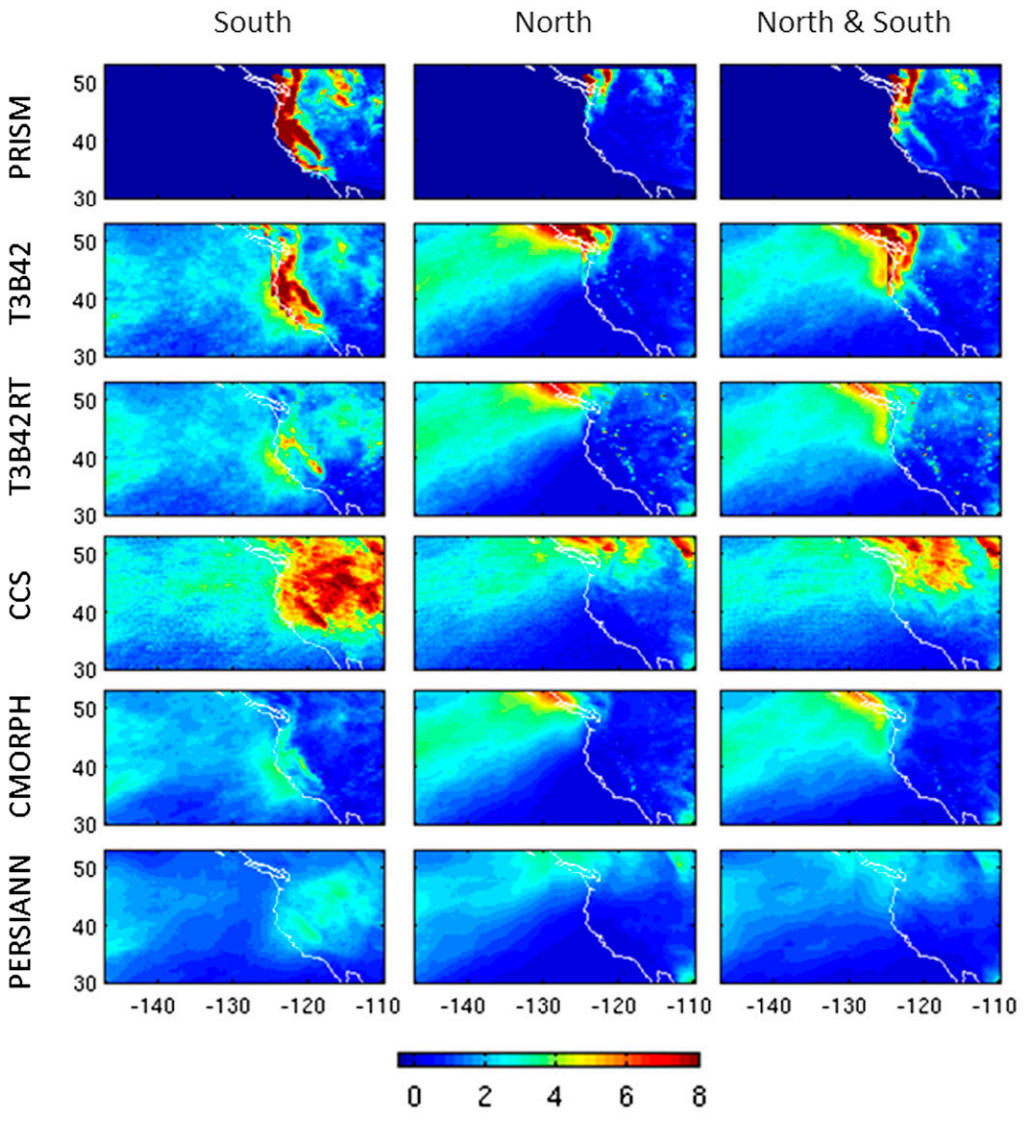

FIG. 2. Maps of mean precipitation rate (mm day^{-1}) in the study domain and for days that the AR database identifies landfalling ARs within the domain bounded by the North American west coast and ~1000 km offshore (see Fig. 1) based on the less stringent landfall criteria (see section 2). From left to right, the columns show maps of mean precipitation rates from the different precipitation products and for ARs that make landfall mainly in California (i.e., 32.5°–41.0°N, designated south); Oregon, Washington, and southern British Columbia (i.e., 40.5°–52.5°N, designated north); and both north and south. The maps are constructed using 10 years of collected ARs (2003–12). Note that (right) does not represent the average of (left) and (middle). It is calculated from ARs identified over both north and south regions.

make landfall in California (i.e., 32.5°–41.0°N; designated south); those that make landfall in Oregon, Washington, and southern British Columbia (i.e., 40.5°–52.5°N; designated north); and those identified as making landfall in north and south. PRISM data are used as a reference for mean precipitation over land. Figure 2 shows that satellite products are fairly consistent in quantifying mean precipitation rate over ocean, although there is a large discrepancy to the west of Washington and southern British Columbia for the north coast results. Over the ocean, PERSIANN represents generally lower mean precipitation rates than the other products, especially in north (Fig. 2, middle) where CMORPH, T3B42, and T3B42RT are higher than both CCS and PERSIANN. Over land, the bias-adjusted T3B42 product shows a fairly good agreement with PRISM. However, the other satellite products do not show much skill in capturing the mean precipitation rate and precipitation pattern

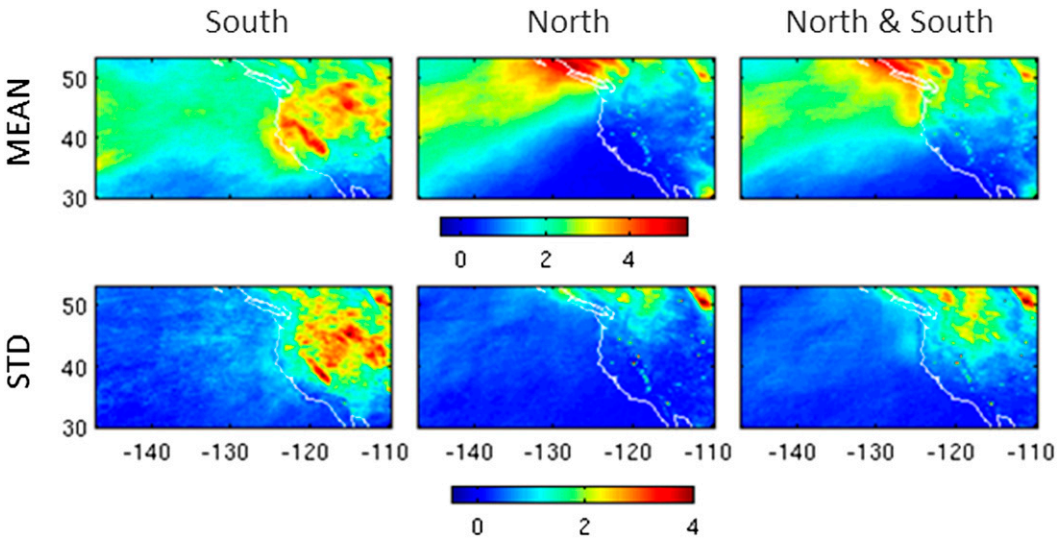

FIG. 3. (top) Mean and (bottom) std dev maps of precipitation rate (mm day^{-1}) calculated from T3B42RT, CMORPH, PERSIANN, and CCS. Similar to Fig. 2, the columns are for designated south, north, and north and south ARs. Note that (right) does not represent the average of (left) and (middle). It is calculated from ARs identified over both north and south regions.

observed from PRISM. CCS shows generally much higher mean precipitation rate than other products, mainly for the north coast, and CMORPH severely underestimates precipitation over land. Note that, as described in section 2, T3B42RT uses climatology for near-real-time bias adjustment. However, Fig. 2 suggests that the bias adjustment is not as effective as that observed in T3B42.

Figure 3 shows maps of mean and standard deviation of precipitation rate calculated from T3B42RT, CCS, CMORPH, and PERSIANN products. The mean and standard deviation maps are calculated after collecting daily maps of precipitation from the four products and, similar to Fig. 2, for those days that the AR database identifies landfalling ARs. T3B42 was not included in calculating the mean and standard deviation as it significantly utilizes rain gauges for bias adjustment over land and thus does not thoroughly represent a satellite-based product. Furthermore, T3B42 and T3B42RT are fairly similar over ocean as there is no rain gauge for bias adjustment. Consistent with that observed in Fig. 2, the products show high agreement over ocean (e.g., low standard deviation) and low agreement over land (e.g., high standard deviation). The maps of mean precipitation rate over land (Fig. 3, top) show some similar patterns to those obtained from the corresponding PRISM maps (Fig. 2, top). Yet, there remain large discrepancies between PRISM and satellite products in capturing the precipitation rates.

Figure 4 is similar to Fig. 2, except AR landfalls are collected using the more stringent landfall criteria (see section 2). In addition, the day of landfall and the day immediately after that are included to assess the entire impact of ARs over land. Furthermore, by utilizing surface temperature data, it was assumed that precipitation over surfaces with 2-m air temperature below 0°C falls as snow. Based on this assumption, the two right columns in Fig. 4 show mean snowfall rates from the studied products. The overall results of comparing precipitation maps are similar to those discussed earlier.

Note that T3B42RT employs climatology data for near-real-time bias adjustment of the precipitation estimate; thus, in a sense it is not a pure satellite product. On the other hand, CMORPH does not retrieve precipitation rate from IR and uses precipitation estimates from MW retrievals exclusively. Over frozen surface, MW precipitation estimates from individual sensors can be missed. In CMORPH, the missed MW precipitation data are assigned to zero if no precipitation is inferred from IR images. However, missing data remain for precipitation events over snow and ice surfaces (R. Joyce 2013, personal communication) and in this study they are not included in the calculation of CMORPH mean precipitation rates. This could be a reason for the significant underestimation of CMORPH precipitation, and especially snowfall, over land (see Figs. 2, 4). Different from CMORPH, T3B42 fills the missing MW estimates with IR-based precipitation data (Huffman et al. 2007).

Figure 5 enables a more detailed comparison of the different products by focusing on region B1 (see Figs. 1b, 5a) that includes California's Sierra Nevada and region B2 (see Figs. 1b, 5b) that covers western Washington

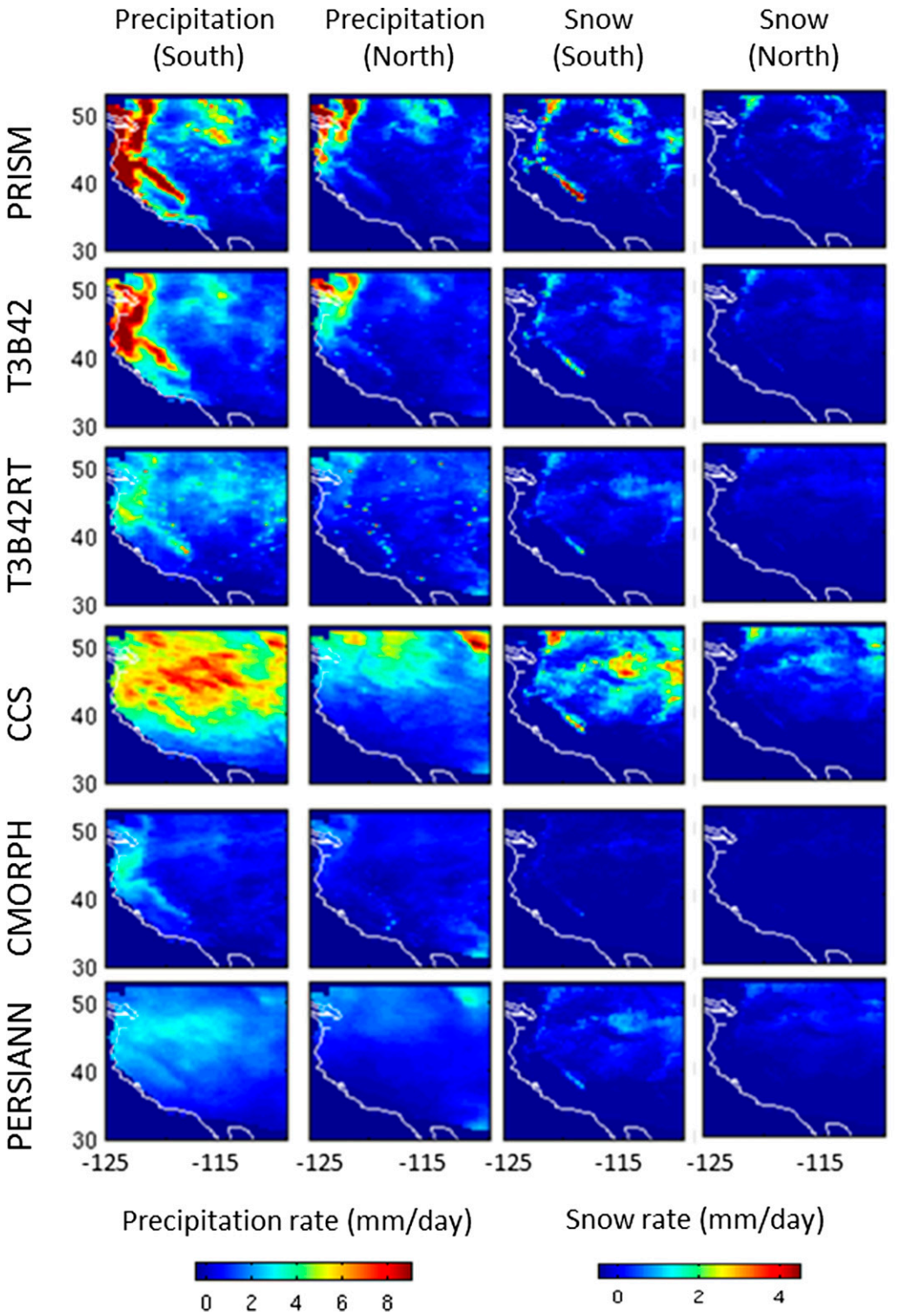

FIG. 4. Maps of mean precipitation rate (mm day^{-1}) over land brought by ARs. These maps were constructed using the different precipitation products (stratified by row) discussed in the text. AR landfalls are based on the more stringent criteria (see section 2). The averaging includes the days of landfall and the day immediately after those. Snowfall maps in the right two columns are constructed from precipitation maps under the assumption that precipitation over surfaces with 2-m air temperature below 0°C falls as snow. The maps are constructed using 10 years of collected ARs (2003–12).

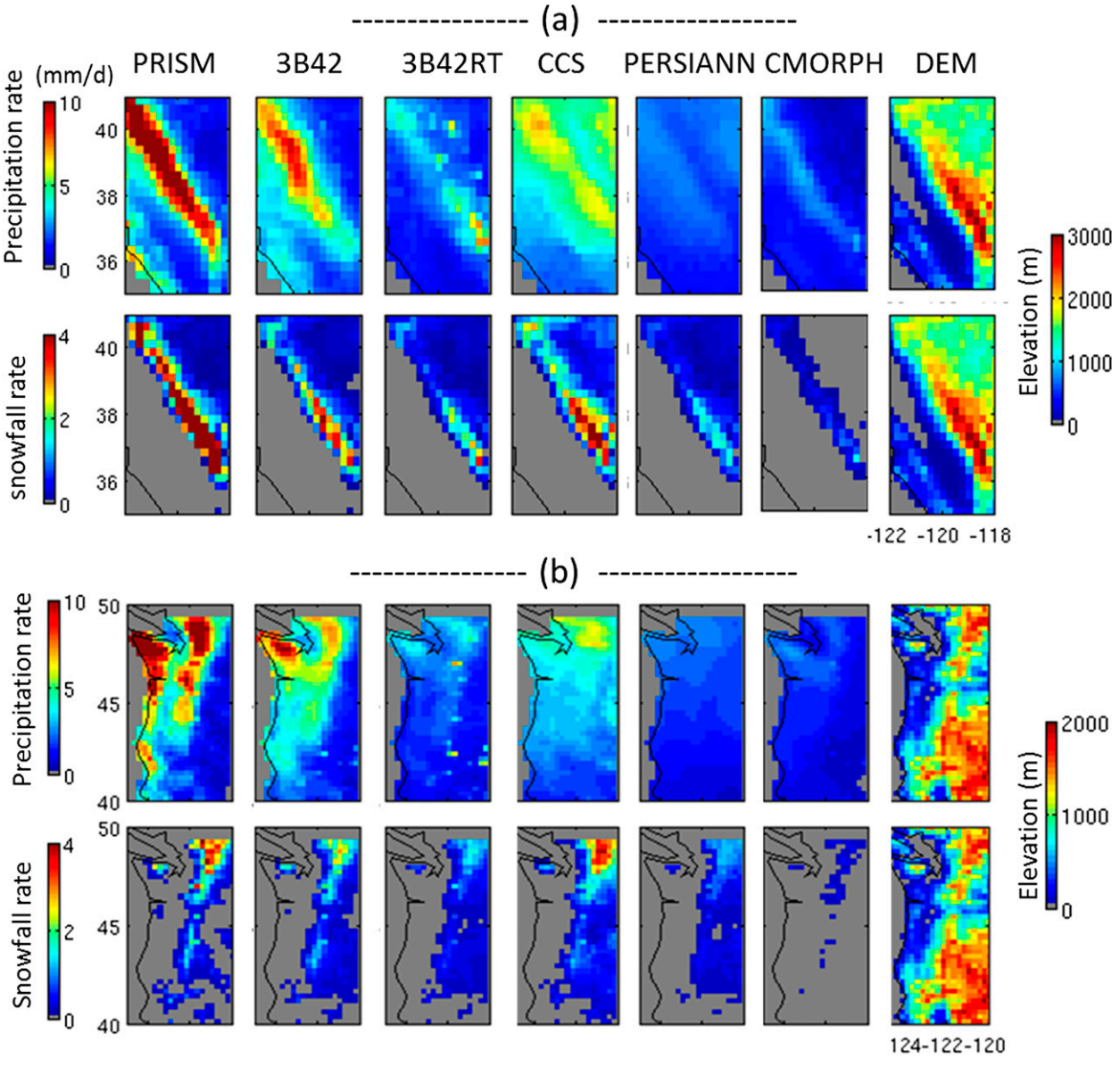

FIG. 5. Maps of mean precipitation rate (mm day^{-1}) over land brought by ARs based on the more stringent criteria over regions (a) B1 and (b) B2 (see Fig. 1b). In (a) and (b), maps are shown of mean precipitation rate (top) and mean snowfall rate (bottom) approximated using precipitation and surface air temperature data. The first column from right shows the corresponding elevation maps (m MSL). The remaining columns show results from the different precipitation products.

and Oregon and far northern California. In Fig. 5a (top) and Fig. 5b (top), the average precipitation rate maps calculated from the entire dataset (2003–12) are shown. In Fig. 5a (bottom) and Fig. 5b (bottom), the maps include only precipitation days on which surface temperature is below 0°C, and thus they approximate maps of average snowfall rate. Corresponding elevation maps are also shown in the last column on the right. Figure 5a shows that average precipitation is highest over and in the vicinity of the Sierra Nevada, likely due to the orographic enhancement of precipitation on the windward side of the mountains (e.g., Dettinger et al. 2004). While mean snowfall is generally higher at higher elevations (Fig. 5a, bottom), the highest rate of mean snowfall does not occur over the highest elevation (Fig. 5a, top). T3B42, followed by CCS, T3B42RT, and CMORPH, shows the highest skill in capturing the location of the intense mean precipitation estimated by PRISM. However, all of the products, especially PERSIANN and CMORPH, significantly underestimate the mean precipitation intensity. As discussed earlier, one major reason for underestimation of CMORPH is related to the missing precipitation data

over snow and frozen lands by various MW products, collectively and exclusively used in CMORPH. This hampers a thorough assessment of CMORPH over these regions. Figure 5a also suggests that CCS overestimates precipitation intensity often at lower elevations compared to PRISM and the other products. However, CCS and PRISM show a fairly good agreement in capturing the location and intensity of snowfall.

Figure 5b compares different products over the Pacific Northwest coast and the western halves of Washington and Oregon. While all the satellite products show significant underestimation of mean precipitation, CCS shows a fairly uniform mean precipitation that often varies between 4 and 6 mm day^{-1}, exceeding PRISM mean precipitation in the east over the Cascade Mountains. Unlike other satellite products, T3B42 shows fairly good skill in capturing the orographic enhancement of precipitation in region B2. Figure 5b (bottom) shows that maps of approximated mean snowfall rate are comparable with PRISM, especially for CCS. Note that the similarity of the mean snowfall pattern among the products can be an artifact of masking precipitation over nonfrozen surfaces. A summary of daily skill scores for precipitation estimates over regions B1 and B2 are provided in Table 1. Bias is defined as the ratio of the total estimated to the total observed values with perfection represented by 1. Clearly, the bias adjustment improves the overall performance of T3B42, relative to the other satellite products. If not bias adjusted, the products show significant underestimation of total precipitation and relatively lower correlation. While CCS maintains a comparable total precipitation over both regions (e.g., bias near 1), precipitation maps (e.g., Figs. 2, 4) and root-mean-square errors (Table 1) suggest that false detection and estimation play a role in improving the overall bias of CCS. Note that CMORPH was not included in the analysis because the product has missing data over snow and frozen surfaces.

A more detailed comparison can be performed by plotting the fractions of precipitation volume (y axis) versus precipitation intensity (x axis) for different products and PRISM as the reference. Figure 6 shows such plots constructed for precipitation rate and snowfall rate, separately for B1 and B2 regions (see Fig. 1). For a fair and more conclusive comparison, CMORPH was not included in the plot, because the product has missing data over snow and frozen surfaces. Figures 6a and 6b show that in both regions the intense precipitation rate is underestimated by satellite products. The bias-adjusted T3B42 product captures the intense part of the precipitation spectrum well, but that is at the expense of deviating from the PRISM histogram in the lower precipitation rates (e.g., compare T3B42 and T3B42RT).

TABLE 1. A summary of daily skill scores for precipitation estimates over regions B1 and B2. COR is correlation coefficient, RMSE is root-mean-square error (mm day^{-1}), and bias is defined as the ratio of the total estimated to the total observed values with perfection represented by 1. PRISM is used as truth.

	Rain			Snow		
Products	COR	RMSE	Bias	COR	RMSE	Bias
Region B1						
T3B42	54.2	9.8	0.87	60.3	4.1	0.50
T3B42RT	38.5	9.5	0.51	46.5	4.7	0.30
CCS	25.9	10.5	0.97	42.3	4.7	0.78
PERSIANN	30.8	9.7	0.46	46.7	4.7	0.26
Region B2						
T3B42	61.4	9.6	0.87	57.8	2.7	0.84
T3B42RT	51.7	8.9	0.46	52.5	2.4	0.58
CCS	35.7	9.8	0.79	49.6	3.0	1.26
PERSIANN	26.9	10.3	0.40	24.6	3.3	0.53

In both regions PERSIANN displays a significant underestimation of the intense precipitation rate and shows more light rain precipitation than PRISM, likely an artifact of a systematic shift of precipitation rates toward the lower end of the spectrum. CCS behaves very differently from the other products over B1 and places a significant fraction of precipitation in the midintensity range between 4 and 40 mm day^{-1}. The plots of snowfall distribution for B1 (Fig. 6c) are fairly consistent with that estimated from PRISM, although a shift toward a less intense rate is noticeable for the solid phase. Figure 6d, however, shows that the satellite products have only little skill in capturing light snowfall compared to PRISM in region B2.

b. *Case study perspective*

Figure 7 shows maps of average precipitation rate that resulted from an atmospheric river that hit northern and central California on 13 and 14 October 2009. This event caused landslides in the coastal Santa Cruz Mountains and in Sequoia National Park in the Sierra Nevada and estimated $10 million in damages (Ralph et al. 2011). Figure 7 shows that satellite products are fairly consistent in locating the precipitation over the ocean and as they hit land, but there are considerable differences among the products in capturing precipitation pattern and intensity. Over land, the products show less skill in capturing the precipitation features estimated by PRISM. In other words, the satellite products significantly underestimate precipitation rate and barely capture the orographic precipitation, especially if not bias adjusted. The observed underestimation can be partly related to the general underestimation of MW and IR sensors from nonconvective precipitation systems that are more often in higher latitudes (Behrangi et al. 2012, 2014). Note that PERSIANN (Fig. 7e) and CMORPH (Fig. 7d) show fairly similar precipitation maps, different

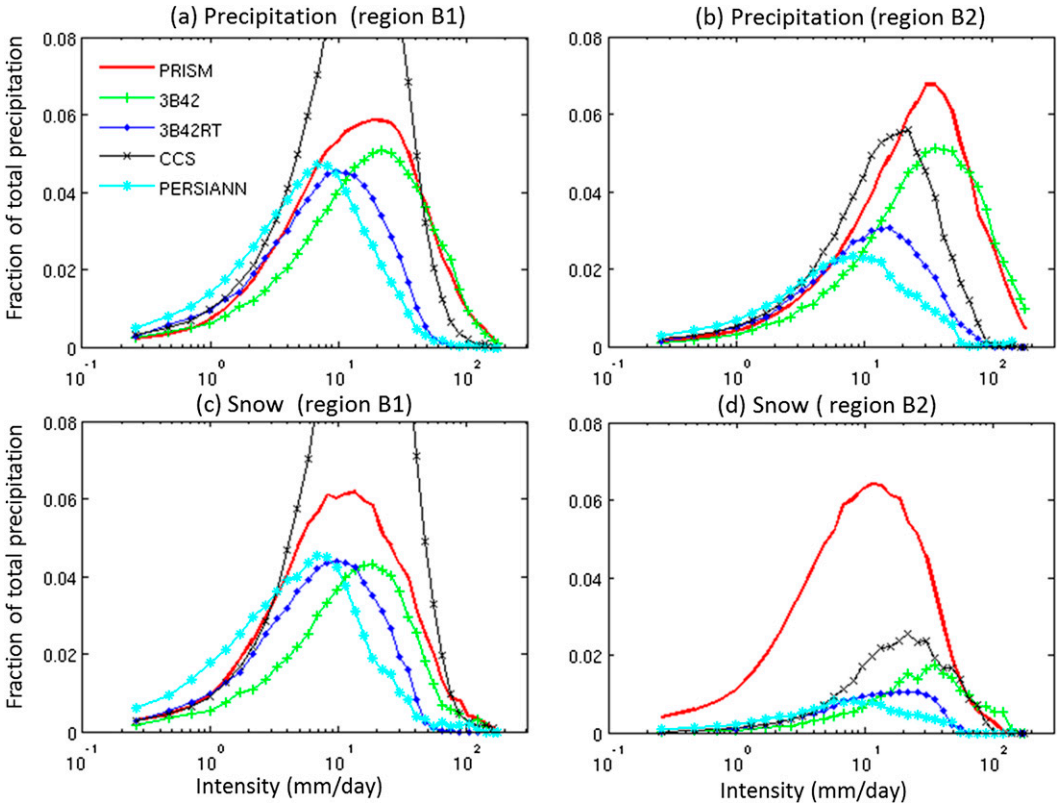

FIG. 6. Distribution of volume of precipitation in regions (a),(c) B1 and (b),(d) B2. The mean precipitation rate (mm day^{-1}) (top) and mean snow rate (mm day^{-1}) (bottom) are given and the area below the PRISM curve is 1.

from that of T3B42 (Fig. 7b), T3B42RT (Fig. 7c), and CCS (Fig. 7f). Interestingly, CCS produces some intense precipitation over the southern Sierra Nevada (Fig. 7f), comparable to that observed by PRISM (Fig. 7a). However, hourly analysis of CCS showed that the large intensity is at least partly related to the presence of a cold surface (Fig. 7h) mistakenly considered as cold precipitating cloud by the IR technique. Furthermore, CCS shows the least precipitation rate over the coastlines, likely due to dominant presence of shallow clouds with cloud-top temperatures above a fixed brightness temperature threshold used in CCS to filter nonprecipitating clouds (Hong et al. 2004).

Figure 8 is similar to Fig. 7, but for an intense AR that impacted western Washington on 6–8 January 2009 (Neiman et al. 2011). The event caused approximately $125 million in damages and led to flooding and the closure of a more than 30-km stretch of Interstate 5 and the closure of Amtrak lines out of Seattle, Washington. By comparing the mean precipitation maps from satellite products (Figs. 8b–f) with PRISM (Fig. 8a), the results are found fairly consistent with the AR case study discussed in Fig. 7. In other words, it was found that the satellite products, other than T3B42, 1) significantly underestimate precipitation rate over land, 2) barely capture the orographic precipitation (Fig. 8a), and 3) have difficulties in retrieving precipitation over cold and frozen surfaces (e.g., missing data in MW retrieval or false estimate from IR methods). T3B42, however, shows that the bias adjustment using gauge data is effective and can resemble overall precipitation features captured by PRISM. Note that T3B42 shows more skill in capturing the 6–8 January 2009 event (Fig. 8) than the 13 and 14 October 2009 event (Fig. 7). The reason for the event-dependent performance of T3B42 needs further investigation to determine if it is related to the quality of gauge networks used for bias adjustment or it is algorithmic (e.g., poor precipitation detection prior to bias adjustment). Figure 8 also shows that T3B42RT (Fig. 8b) captures some feature of orographic precipitation, but not as effective as T3B42. CCS shows skill in capturing the orographic precipitation, but also shows significant false estimate in northeastern Washington.

5. Concluding remarks

Atmospheric rivers (ARs) are important weather phenomena that need to be better understood in a

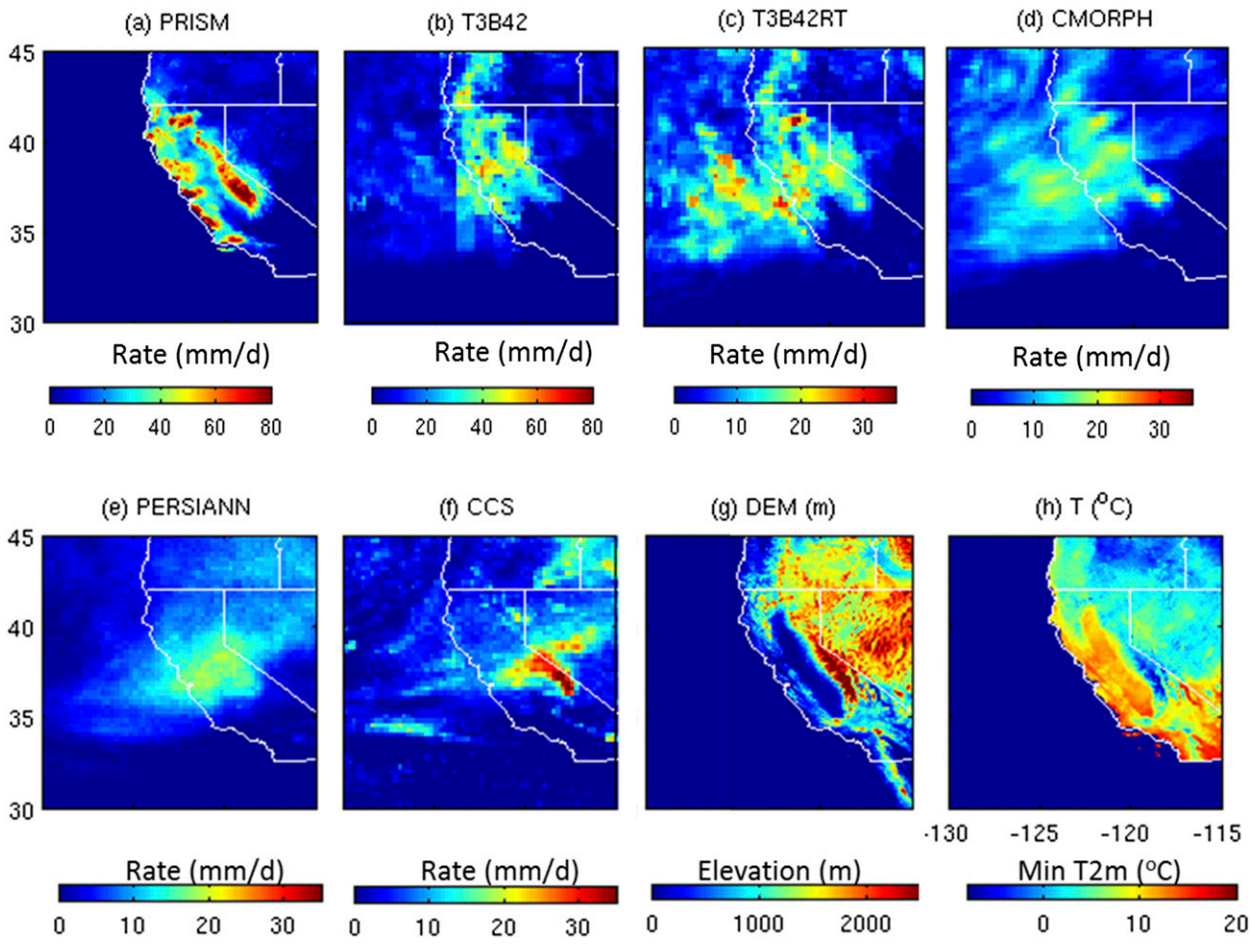

FIG. 7. Maps of mean precipitation rate (mm day^{-1}) resulting from an AR that hit northern and central California on 13 and 14 Oct 2009: (a)–(f) mean precipitation rate from the different products, (g) elevation above sea surface level, and (h) average min 2-m temperature during the event.

changing climate (Dettinger 2011; Lavers et al. 2013; Warner et al. 2015). Their important contributions to precipitation and associated hydrological impacts such as flood and drought, as discussed in the introduction, highlight the need to better quantify the total amount and intensity of precipitation associated with ARs, especially those making landfall. Some specific features of AR weather systems (e.g., precipitation over cold surfaces and topographic interactions), however, present a challenge to satellite retrievals of AR precipitation. A decade (2003–12) of landfalling ARs on the North American west coast are collected to assess the skill of five commonly used satellite-based precipitation products—T3B42, T3B42RT, CMORPH, PERSIANN, and CCS—in capturing ARs' precipitation rate and pattern. In addition, ground-based estimates of precipitation and temperature from PRISM, and topography maps, were used for more detailed analysis.

By analysis of an ensemble of ARs as well as individual case studies, it was found that the satellite products often underestimate precipitation rate over land, barely capture the orographic precipitation, and have difficulties in retrieving precipitation over cold and frozen surfaces (e.g., missing data in microwave retrieval or false detection and estimation from IR methods).

Because of the importance of accurate quantification of precipitation from ARs and lack of sufficient ground observation, especially over ocean and remote areas over land, it is important to improve the quality of the current satellite precipitation products to better retrieve precipitation from ARs. The performance of T3B42 compared to the other products suggests that, in parallel to the development of retrieval techniques and more capable sensors, it is critical to consider timely inclusion of in situ precipitation data in the production of merged precipitation products. Improvement in retrieval of

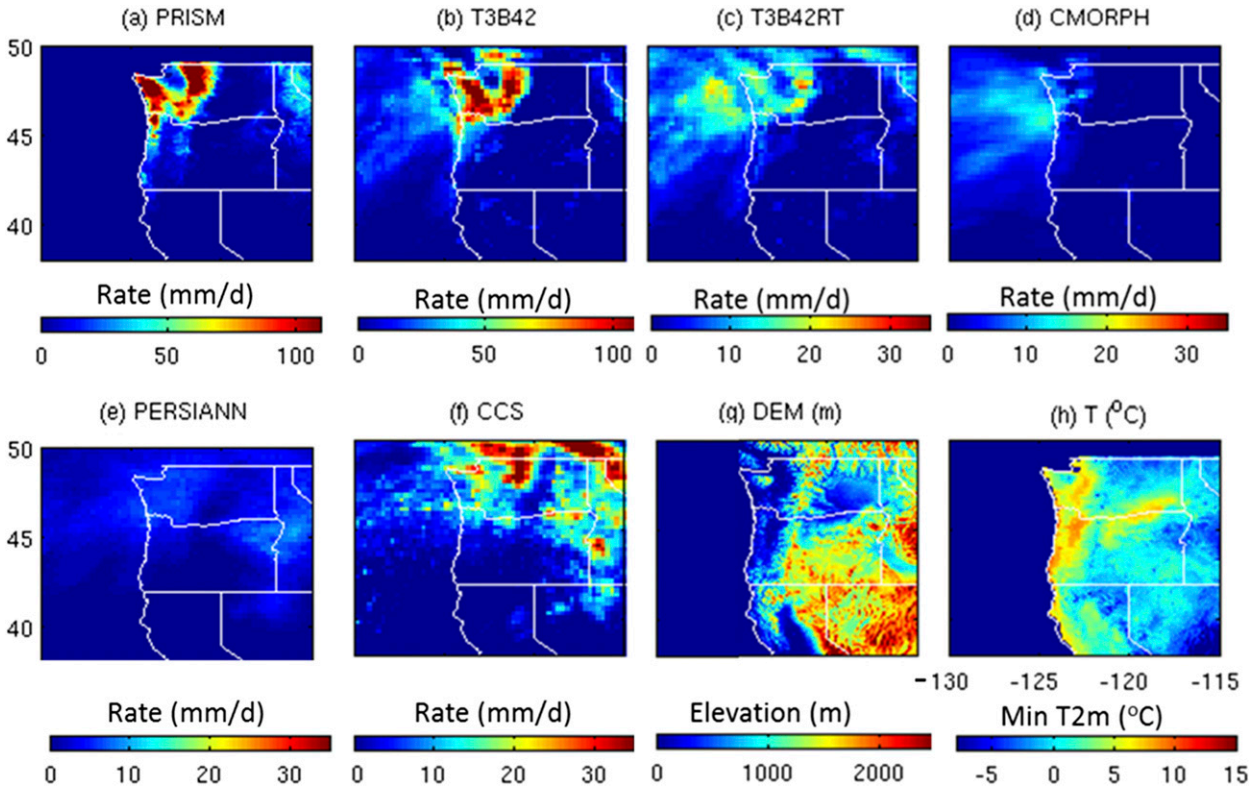

FIG. 8. Maps of mean precipitation rate (mm day^{-1}) resulting from an AR that impacted western Washington on 6–8 Jan 2009: (a)–(f) mean precipitation rate from the different products, (g) elevation above sea surface level, and (h) average min 2-m temperature during the event.

orographic precipitation (e.g., Taniguchi et al. 2013; Shige et al. 2013) is another important area of study that can improve remote sensing of precipitation over the western United States, where ARs together with orographic lifting often cause intense precipitation.

Further advancement in quantifying and monitoring AR precipitation is expected through the Global Precipitation Measurement (GPM) mission (Hou et al. 2014), offering more advanced observing sensors and methods for precipitation retrievals over land and ocean. The Integrated Multisatellite Retrievals for GPM (IMERG; Huffman et al. 2015), released in early 2015, provides timely observation of precipitation at 0.1° × 0.1° resolution every 30 min within the latitude band 60°N–60°S. Efforts are underway to assess the impact of GPM in enhancing AR precipitation retrievals.

Acknowledgments. The research described in this paper was carried out at the Jet Propulsion Laboratory, California Institute of Technology, under a contract with the National Aeronautics and Space Administration. Financial support is also made available from NASA New Investigator Program (NIP), Energy and Water Cycle Study (NEWS), and Weather program awards. Government sponsorship is acknowledged.

REFERENCES

Behrangi, A., K. Hsu, B. Imam, S. Sorooshian, G. J. Huffman, and R. J. Kuligowski, 2009: PERSIANN-MSA: A precipitation estimation method from satellite-based multispectral analysis. *J. Hydrometeor.*, **10**, 1414–1429, doi:10.1175/2009JHM1139.1.

——, B. Imam, K. Hsu, S. Sorooshian, T. J. Bellerby, and G. J. Huffman, 2010: REFAME: Rain Estimation Using Forward-Adjusted Advection of Microwave Estimates. *J. Hydrometeor.*, **11**, 1305–1321, doi:10.1175/2010JHM1248.1.

——, M. Lebsock, S. Wong, and B. Lambrigtsen, 2012: On the quantification of oceanic rainfall using spaceborne sensors. *J. Geophys. Res.*, **117**, D20105, doi:10.1029/2012JD017979.

——, Y. Tian, B. H. Lambrigtsen, and G. L. Stephens, 2014: What does *CloudSat* reveal about global land precipitation detection by other spaceborne sensors? *Water Resour. Res.*, **50**, 4893–4905, doi:10.1002/2013WR014566.

Daly, C., W. P. Gibson, G. H. Taylor, G. L. Johnson, and P. Pasteris, 2002: A knowledge-based approach to the statistical mapping of climate. *Climate Res.*, **22**, 99–113, doi:10.3354/cr022099.

Dettinger, M. D., 2011: Climate change, atmospheric rivers, and floods in California—A multimodel analysis of storm frequency and magnitude changes. *J. Amer. Water Resour. Assoc.*, **47**, 514–523, doi:10.1111/j.1752-1688.2011.00546.x.

——, 2013: Atmospheric rivers as drought busters on the U.S. West Coast. *J. Hydrometeor.*, **14**, 1721–1732, doi:10.1175/JHM-D-13-02.1.

——, K. Redmond, and D. Cayan, 2004: Winter orographic precipitation ratios in the Sierra Nevada—Large-scale atmospheric circulations and hydrologic consequences. *J. Hydrometeor.*, **5**, 1102–1116, doi:10.1175/JHM-390.1.

——, F. M. Ralph, T. Das, P. J. Neiman, and D. R. Cayan, 2011: Atmospheric rivers, floods and the water resources of California. *Water*, **3**, 445–478, doi:10.3390/w3020445.

Ferraro, R. R., F. H. Weng, N. C. Grody, and L. M. Zhao, 2000: Precipitation characteristics over land from the *NOAA-15* AMSU sensor. *Geophys. Res. Lett.*, **27**, 2669–2672, doi:10.1029/2000GL011665.

——, and Coauthors, 2013: An evaluation of microwave land surface emissivities over the continental United States to benefit GPM-era precipitation algorithms. *IEEE Trans. Geosci. Remote Sens.*, **51**, 378–398, doi:10.1109/TGRS.2012.2199121.

Gimeno, L., R. Nieto, M. Vázquez, and D. A. Lavers, 2014: Atmospheric rivers: A mini-review. *Front. Earth Sci.*, **2**, doi:10.3389/feart.2014.00002.

Guan, B., N. P. Molotch, D. E. Waliser, E. J. Fetzer, and P. J. Neiman, 2010: Extreme snowfall events linked to atmospheric rivers and surface air temperature via satellite measurements. *Geophys. Res. Lett.*, **37**, L20401, doi:10.1029/2010GL044696.

——, ——, ——, ——, and ——, 2013: The 2010/2011 snow season in California's Sierra Nevada: Role of atmospheric rivers and modes of large-scale variability. *Water Resour. Res.*, **49**, 6731–6743, doi:10.1002/wrcr.20537.

Haddad, Z. S., E. A. Smith, C. D. Kummerow, T. Iguchi, M. R. Farrar, S. L. Durden, M. Alves, and W. S. Olson, 1997: The TRMM 'day-1' radar/radiometer combined rain-profiling algorithm. *J. Meteor. Soc. Japan*, **75**, 799–809.

Hong, Y., K. L. Hsu, S. Sorooshian, and X. G. Gao, 2004: Precipitation Estimation from Remotely Sensed Imagery using an Artificial Neural Network Cloud Classification System. *J. Appl. Meteor.*, **43**, 1834–1852, doi:10.1175/JAM2173.1.

Hou, A. Y., and Coauthors, 2014: The Global Precipitation Measurement Mission. *Bull. Amer. Meteor. Soc.*, **95**, 701–722, doi:10.1175/BAMS-D-13-00164.1.

Hsu, K. L., X. G. Gao, S. Sorooshian, and H. V. Gupta, 1997: Precipitation estimation from remotely sensed information using artificial neural networks. *J. Appl. Meteor.*, **36**, 1176–1190, doi:10.1175/1520-0450(1997)036<1176:PEFRSI>2.0.CO;2.

Huffman, G. J., and D. T. Bolvin, 2014: TRMM and other data precipitation data set documentation. NASA GSFC, 42 pp. [Available online at ftp://precip.gsfc.nasa.gov/pub/trmmdocs/3B42_3B43_doc.pdf.]

——, and Coauthors, 2007: The TRMM Multisatellite Precipitation Analysis (TMPA): Quasi-global, multiyear, combined-sensor precipitation estimates at fine scales. *J. Hydrometeor.*, **8**, 38–55, doi:10.1175/JHM560.1.

——, D. Bolvin, and E. Nelkin, 2015: Integrated Multi-Satellite Retrievals for GPM (IMERG) technical documentation. IMERG Tech. Doc., NASA GSFC, 48 pp. [Available online at http://pmm.nasa.gov/sites/default/files/document_files/IMERG_doc.pdf.]

Joyce, R. J., J. E. Janowiak, P. A. Arkin, and P. Xie, 2004: CMORPH: A method that produces global precipitation estimates from passive microwave and infrared data at high spatial and temporal resolution. *J. Hydrometeor.*, **5**, 487–503, doi:10.1175/1525-7541(2004)005<0487:CAMTPG>2.0.CO;2.

Kidd, C., D. R. Kniveton, M. C. Todd, and T. J. Bellerby, 2003: Satellite rainfall estimation using combined passive microwave and infrared algorithms. *J. Hydrometeor.*, **4**, 1088–1104, doi:10.1175/1525-7541(2003)004<1088:SREUCP>2.0.CO;2.

Kim, J., D. E. Waliser, P. J. Neiman, B. Guan, J.-M. Ryoo, and G. A. Wick, 2013: Effects of atmospheric river landfalls on the cold season precipitation in California. *Climate Dyn.*, **40**, 465–474, doi:10.1007/s00382-012-1322-3.

Kongoli, C., P. Pellegrino, R. R. Ferraro, N. C. Grody, and H. Meng, 2003: A new snowfall detection algorithm over land using measurements from the Advanced Microwave Sounding Unit (AMSU). *Geophys. Res. Lett.*, **30**, 1756, doi:10.1029/2003GL017177.

Kuligowski, R. J., 2002: A self-calibrating real-time GOES rainfall algorithm for short-term rainfall estimates. *J. Hydrometeor.*, **3**, 112–130, doi:10.1175/1525-7541(2002)003<0112:ASCRTG>2.0.CO;2.

Lavers, D. A., and G. Villarini, 2013: The nexus between atmospheric rivers and extreme precipitation across Europe. *Geophys. Res. Lett.*, **40**, 3259–3264, doi:10.1002/grl.50636.

——, R. P. Allan, G. Villarini, B. Lloyd-Hughes, D. J. Brayshaw, and A. J. Wade, 2013: Future changes in atmospheric rivers and their implications for winter flooding in Britain. *Environ. Res. Lett.*, **8**, 034010, doi:10.1088/1748-9326/8/3/034010.

Liu, C., and E. J. Zipser, 2009: "Warm rain" in the tropics: Seasonal and regional distributions based on 9 yr of TRMM data. *J. Climate*, **22**, 767–779, doi:10.1175/2008JCLI2641.1.

Lundquist, J. D., P. J. Neiman, B. Martner, A. B. White, D. J. Gottas, and F. M. Ralph, 2008: Rain versus snow in the Sierra Nevada, California: Comparing Doppler profiling radar and surface observations of melting level. *J. Hydrometeor.*, **9**, 194–211, doi:10.1175/2007JHM853.1.

Martner, B. E., S. E. Yuter, A. B. White, S. Y. Matrosov, D. E. Kingsmill, and F. M. Ralph, 2008: Raindrop size distributions and rain characteristics in California coastal rainfall for periods with and without a radar bright band. *J. Hydrometeor.*, **9**, 408–425, doi:10.1175/2007JHM924.1.

Matrosov, S. Y., 2012: Observations of wintertime U.S. West Coast precipitating systems with W-band satellite radar and other spaceborne instruments. *J. Hydrometeor.*, **13**, 223–238, doi:10.1175/JHM-D-10-05025.1.

——, 2013: Characteristics of landfalling atmospheric rivers inferred from satellite observations over the eastern North Pacific Ocean. *Mon. Wea. Rev.*, **141**, 3757–3768, doi:10.1175/MWR-D-12-00324.1.

Neiman, P. J., G. A. Wick, F. M. Ralph, B. E. Martner, A. B. White, and D. E. Kingsmill, 2005: Wintertime nonbrightband rain in California and Oregon during CALJET and PACJET: Geographic, interannual, and synoptic variability. *Mon. Wea. Rev.*, **133**, 1199–1223, doi:10.1175/MWR2919.1.

——, F. M. Ralph, G. A. Wick, J. D. Lundquist, and M. D. Dettinger, 2008: Meteorological characteristics and overland precipitation impacts of atmospheric rivers affecting the west coast of North America based on eight years of SSM/I satellite observations. *J. Hydrometeor.*, **9**, 22–47, doi:10.1175/2007JHM855.1.

——, L. J. Schick, F. M. Ralph, M. Hughes, and G. A. Wick, 2011: Flooding in western Washington: The connection to atmospheric rivers. *J. Hydrometeor.*, **12**, 1337–1358, doi:10.1175/2011JHM1358.1.

Ralph, F. M., P. J. Neiman, and G. A. Wick, 2004: Satellite and CALJET aircraft observations of atmospheric rivers over the eastern North Pacific Ocean during the winter of 1997/98. *Mon. Wea. Rev.*, **132**, 1721–1745, doi:10.1175/1520-0493(2004)132<1721:SACAOO>2.0.CO;2.

——, ——, ——, S. I. Gutman, M. D. Dettinger, D. R. Cayan, and A. B. White, 2006: Flooding on California's Russian River: Role of atmospheric rivers. *Geophys. Res. Lett.*, **33**, L13801, doi:10.1029/2006GL026689.

——, ——, G. N. Kiladis, K. Weickman, and D. W. Reynolds, 2011: A multi-scale observational case study of a Pacific atmospheric river exhibiting tropical–extratropical connections and a mesoscale frontal wave. *Mon. Wea. Rev.*, **139**, 1169–1189, doi:10.1175/2010MWR3596.1.

Shige, S., S. Kida, H. Ashiwake, T. Kubota, and K. Aonashi, 2013: Improvement of TMI rain retrievals in mountainous areas. *J. Appl. Meteor. Climatol.*, **52**, 242–254, doi:10.1175/JAMC-D-12-074.1.

Sorooshian, S., K. L. Hsu, X. Gao, H. V. Gupta, B. Imam, and D. Braithwaite, 2000: Evaluation of PERSIANN system satellite-based estimates of tropical rainfall. *Bull. Amer. Meteor. Soc.*, **81**, 2035–2046, doi:10.1175/1520-0477(2000)081<2035:EOPSSE>2.3.CO;2.

Stohl, A., C. Forster, and H. Sodemann, 2008: Remote sources of water vapor forming precipitation on the Norwegian west coast at 60°N—A tale of hurricanes and an atmospheric river. *J. Geophys. Res.*, **113**, D05102, doi:10.1029/2007JD009006.

Taniguchi, A., and Coauthors, 2013: Improvement of high-resolution satellite rainfall product for Typhoon Morakot (2009) over Taiwan. *J. Hydrometeor.*, **14**, 1859–1871, doi:10.1175/JHM-D-13-047.1.

Viale, M., and M. N. Nuñez, 2011: Climatology of winter orographic precipitation over the subtropical central Andes and associated synoptic and regional characteristics. *J. Hydrometeor.*, **12**, 481–507, doi:10.1175/2010JHM1284.1.

Vila, D., R. Ferraro, and R. Joyce, 2007: Evaluation and improvement of AMSU precipitation retrievals. *J. Geophys. Res.*, **112**, D20119, doi:10.1029/2007JD008617.

Warner, M. D., C. F. Mass, and E. P. Salathé Jr., 2012: Wintertime extreme precipitation events along the Pacific Northwest coast: Climatology and synoptic evolution. *Mon. Wea. Rev.*, **140**, 2021–2043, doi:10.1175/MWR-D-11-00197.1.

——, ——, and ——, 2015: Changes in winter atmospheric rivers along the North American west coast in CMIP5 climate models. *J. Hydrometeor.*, **16**, 118–128, doi:10.1175/JHM-D-14-0080.1.

Weng, F. Z., L. M. Zhao, R. R. Ferraro, G. Poe, X. F. Li, and N. C. Grody, 2003: Advanced microwave sounding unit cloud and precipitation algorithms. *Radio Sci.*, **38**, 8068, doi:10.1029/2002RS002679.

Zhu, Y., and R. E. Newell, 1994: Atmospheric rivers and bombs. *Geophys. Res. Lett.*, **21**, 1999–2002, doi:10.1029/94GL01710.

——, and ——, 1998: A proposed algorithm for moisture fluxes from atmospheric rivers. *Mon. Wea. Rev.*, **126**, 725–735, doi:10.1175/1520-0493(1998)126<0725:APAFMF>2.0.CO;2.